

**Structural probe of a glass-forming liquid: Generalized compressibility**

Hervé M. Carruzzo\* and Clare C. Yu

*Department of Physics and Astronomy, University of California Irvine, Irvine, California 92697*

(Received 15 December 2001; revised manuscript received 29 March 2002; published 26 August 2002)

We introduce a structural quantity to probe the glass transition. This quantity is a linear generalized compressibility which depends solely on the positions of the particles. We have performed a molecular dynamics simulation on a glass-forming liquid consisting of a two-component mixture of soft spheres in three dimensions. As the temperature is lowered (or as the density is increased), the generalized compressibility drops sharply at the glass transition, with the drop becoming more and more abrupt as the measurement time increases. At our longest measurement times, the drop occurs approximately at the mode coupling temperature  $T_C$ . The drop in the linear generalized compressibility occurs at the same temperature as the peak in the specific heat. By examining the inherent structure energy as a function of temperature, we find that our results are consistent with the kinetic view of the glass transition in which the system falls out of equilibrium. We find no size dependence and no evidence for a second order phase transition, though this does not exclude the possibility of a phase transition below the observed glass transition temperature. We discuss the relation between the linear generalized compressibility and the ordinary isothermal compressibility, as well as the static structure factor.

DOI: 10.1103/PhysRevE.66.021204

PACS number(s): 64.70.Pf, 61.43.Fs, 02.70.Ns, 05.20.-y

**I. INTRODUCTION**

The glass transition is still not well understood despite extensive study. There have been two main theoretical approaches to the problem: dynamic and thermodynamic. Theories in the first category view the glass transition as a kinetic phenomenon characterized by a growing relaxation time and viscosity [1–5]. When the relaxation time exceeds the measurement time, particle motion appears to be arrested resulting in the glass transition. One of the most prominent theories espousing this view is the mode coupling theory in which ideally the relaxation time diverges at a temperature  $T_C$  above the experimental glass transition temperature [3]. Interesting and fruitful concepts such as dynamic inhomogeneities [4,6,7] and the influence of the energy landscape on relaxation processes [8,9] have resulted from this approach. The thermodynamic viewpoint attributes the glass transition to an underlying phase transition hidden from direct experimental observation by extremely long relaxation times [1,2,10–12]. In most scenarios there is an underlying second order phase transition associated with a growing correlation length which produces diverging relaxation times as well as diverging static susceptibilities [13–18]. More recently, Mezard and Parisi [12,19] have argued that the underlying transition is actually a random first order transition signaled by a jump discontinuity in the specific heat.

Experimentally, the glass transition is characterized by both kinetic and thermodynamic features. For example, in the supercooled liquid, kinetic quantities such as the viscosity and relaxation time grow rapidly as the temperature is lowered. When the system falls out of equilibrium below a certain temperature, thermodynamic quantities exhibit features reflecting the glass transition. For example, as the system is cooled the specific heat has a steplike form and the

dielectric constant exhibits a peak at a frequency dependent temperature.

In an effort to better characterize the glass transition, we introduce a structural probe which we call a generalized compressibility [20]. Unlike the specific heat which monitors energy fluctuations, this linear compressibility is a function of the microscopic structure of the system: it depends solely on the positions of the particles and not on their previous history. Since we do not need to compare the system's state at different times, it is not a dynamic or kinetic quantity. Rather it is a thermodynamic quantity in the sense that it is purely a function of the microstate of the system dictated by its location in phase space. The generalized compressibility is easy to compute numerically, and it is simpler than the dielectric constant which involves both the translation and orientation of electric dipoles. In addition, it does not suffer from finite size effects that can often plague measurements of the ordinary compressibility deduced from simulations. The generalized compressibility can be calculated in either the canonical or grand canonical ensembles. In particular, it is well defined for a system with fixed volume  $V$  and particle number  $N$  in contrast to the ordinary compressibility which is defined for a system that has fluctuations in  $N$  or  $V$ . The generalized compressibility should be directly measurable experimentally in colloidal suspensions of polystyrene spheres [21] and possibly in other systems as well. In this paper we present measurements of this quantity in a molecular dynamics simulation of a two-component system of soft spheres. We find that the linear generalized compressibility drops sharply as the temperature decreases below the glass transition temperature  $T_g$ . The drop becomes more and more abrupt as the measurement time increases. This is consistent with the structural arrest associated with a kinetic transition in which the system falls out of equilibrium. Similar results are seen as the density is increased at fixed temperature.

The paper is organized as follows. Section II describes the molecular dynamics simulations. Section III describes how

\*Present address: Internap, Seattle, WA 98101.

the relaxation times and mode coupling  $T_C$  are determined. These are useful for setting the time and temperature scales. Section IV describes our specific heat measurements which show a peak at the glass transition. Section V derives the expressions for the linear and nonlinear generalized compressibilities, and shows our results for these quantities. The linear generalized compressibility shows an abrupt drop at the same temperature and density as the peak in the specific heat. Section VI compares the ordinary isothermal compressibility with our linear generalized compressibility and shows the advantages of the latter. Section VII gives our results for the diffusion constant. Section VIII explains the relation between the linear generalized compressibility and the static structure factor. Finally, we summarize our results in Sec. IX. A brief description of some of these results as well as results for a single component fluid that forms a crystal was reported earlier [22].

## II. MOLECULAR DYNAMICS SIMULATION

We have performed a molecular dynamics simulation on a glass-forming liquid [23,24] consisting of a 50:50 binary mixture of soft spheres in three dimensions. The two types of spheres, labeled  $A$  and  $B$ , differ only in their sizes. The interaction between two particles a distance  $r$  apart is given by  $V_{\alpha\beta}(r) = \epsilon[(\sigma_{\alpha\beta}/r)^{12} + X_{\alpha\beta}(r)]$ , where the interaction length  $\sigma_{\alpha\beta} = (\sigma_\alpha + \sigma_\beta)/2$  with  $\sigma_B/\sigma_A = 1.4$  ( $\alpha, \beta = A, B$ ). For numerical efficiency, we set the cutoff function  $X_{\alpha\beta}(r) = r/\sigma_{\alpha\beta} - \lambda$  with  $\lambda = 13/12^{12/13}$ . The interaction is cutoff at the minimum of the potential  $V_{\alpha\beta}(r)$ . Energy and length are measured in units of  $\epsilon$  and  $\sigma_A$ , respectively. Temperature is given in units of  $\epsilon/k_B$  where  $k_B$  is the Boltzmann's constant, and time is in units of  $\sigma_A \sqrt{m/\epsilon}$  where  $m$ , the mass of the particles, is set to unity. The equations of motion were integrated using the leapfrog method [25] with a time step of 0.005. During each run, the average density  $\rho_o = N/L^3$  was fixed, and the temperature was kept constant using a constraint algorithm [25]. The volume  $V = L^3$ .  $N = N_A + N_B$  is the total number of particles. The system occupies a cube with dimensions  $(\pm L/2, \pm L/2, \pm L/2)$  and periodic boundary conditions.

We have done sweeps of both temperature and density. We fix the parameters so that crystallization is avoided upon cooling or when the density is increased. For the temperature sweeps, we fix the density at  $\rho_o = 0.6$ . For  $\sigma_B/\sigma_A = 1.4$ , this corresponds to a packing fraction of 1.04. Having a packing fraction larger than 1 means that each particle was interacting with other particles most, if not all, of the time. Our measuring procedure is the following. For runs where we cool the system, we start each run at a high temperature ( $T = 1.5$ ) and lower the temperature in steps of  $\Delta T = 0.05$ . At each temperature we equilibrate for  $10^4$  molecular dynamics steps (MD steps) and then measure the quantities of interest for  $N_\tau$  additional MD steps where  $N_\tau = 10^5, 2 \times 10^5, 10^6, 3 \times 10^6$ , or  $10^7$ . All the particles move at each MD step. The results are then averaged over up to 40 different initial conditions (different initial positions and velocities of the spheres). We have done some runs in which we heat the system of particles by starting at our lowest temperature  $T$

$= 0.1$  with a configuration obtained by cooling the system. We then increased the temperature in steps of  $\Delta T = 0.05$ . As before, we equilibrate at each temperature for  $10^4$  time steps and then measure quantities for an additional  $10^6$  time steps.

We have also done some density sweeps in which we fix the temperature ( $T = 1.0$ ) and systematically change the density. The glass transition occurs as we increase the density. Colloidal experiments often study the glass transition as a function of density. We start each run at a low density ( $\rho = 0.4$ ) and increase the density in steps of  $\Delta\rho = 0.025$ . At each density we equilibrate for  $10^4$  MD steps and then measure the quantities of interest for  $N_\tau$  additional MD steps.

The glass transition occurs either as the temperature is lowered or as the density is raised. It is worth noting that temperature and density can be combined into a dimensionless parameter  $\Gamma$  [26],

$$\Gamma = \rho \sigma_{eff}^3 / T^{1/4}, \quad \sigma_{eff}^3 = \sum_{\alpha\beta} n_\alpha n_\beta \sigma_{\alpha\beta}^3, \quad (1)$$

where  $\sigma_{eff}$  represents an effective diameter for particles in the mixture. The concentration of each type of particle is given by  $n_A = N_A/N$  and  $n_B = 1 - n_A$ . For our simulations  $n_A = n_B = 0.5$ .  $\Gamma$  is the relevant parameter when the particles spend most of their time sampling a nonzero interparticle potential, i.e., for  $\rho^{-1/3} < \sigma_{eff}$ . Thus  $\Gamma$  is particularly useful for interparticle interactions which fall off with distance as a power law and do not have a cutoff beyond which the interaction is zero. When cooling from the liquid phase, the glass transition is known to occur around  $\Gamma = 1.45$  [26].

We have looked for phase separation of the two types of spheres by examining the distribution of large and small spheres in the neighborhood of large spheres and in the neighborhood of small spheres. We see no evidence for phase separation at either high ( $T = 1.5$ ) or low ( $T = 0.15$ ) temperatures at a density of  $\rho = 0.6$ .

## III. RELAXATION TIMES AND MODE COUPLING $T_C$

As points of reference for the time and temperature scales, it is useful to find the mode coupling  $T_C$  and the  $\alpha$  relaxation times. We can find the relaxation times using the intermediate scattering function  $F(\vec{k}, t)$  which is a useful probe of the structural relaxation. It is the spatial Fourier transform of the van Hove correlation function  $G(\vec{r}, t)$  and the inverse time transform of the dynamic structure factor  $S(\vec{k}, \omega)$ . There are two different types of intermediate scattering function: the self (incoherent) intermediate scattering function  $F_s(\vec{k}, t)$  and the full (coherent) intermediate scattering function  $F(\vec{k}, t)$ .

In a computer simulation, the self (incoherent) part of the partial intermediate scattering function  $F_{s,\alpha}(\vec{k}, t)$  can be calculated directly using [27]

$$F_{s,\alpha}(\vec{k}, t) = \frac{1}{N_\alpha} \left\langle \sum_{i=1}^{N_\alpha} e^{i\vec{k} \cdot [\vec{r}_i(t) - \vec{r}_i(0)]} \right\rangle, \quad (2)$$

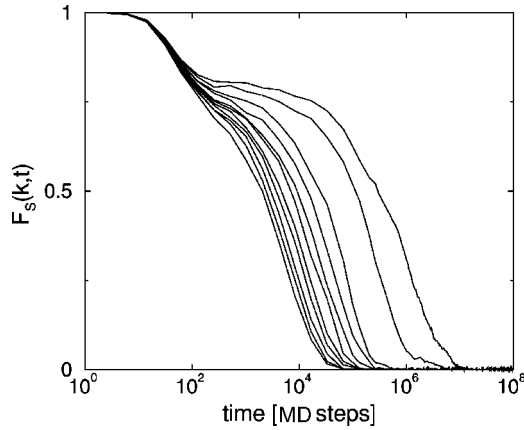


FIG. 1. The self-intermediate scattering function vs time for a system with 512 particles and  $\rho_o=0.6$ . The time is given in units of molecular dynamics (MD) time steps. From left to right, the curves are for temperatures  $T=0.381\ 679$ ,  $0.373\ 134$ ,  $0.364\ 964$ ,  $0.357\ 143$ ,  $0.349\ 65$ ,  $0.342\ 466$ ,  $0.335\ 57$ ,  $0.328\ 947$ ,  $0.321\ 543$ ,  $0.302\ 114\ 8$ , and  $0.289\ 855$ , respectively. 256 type  $B$  particles were used and the wave vector  $k=2\pi\times 8.3666/L$ , which is the location of the first peak in the structure factor for type  $B$  particles,  $L=8$ . For each curve the system was initialized from a configuration at that temperature obtained from parallel tempering which is described in the Appendix. Then the simulation was run only at that temperature. The temperatures were chosen so that the parallel tempering acceptance rates were high. The curves at the seven highest temperatures were equilibrated for  $1\times 10^6$  MD time steps before recording the configurations used to calculate  $F_s(k,t)$ . Each curve of the seven highest temperature curves is averaged over 24 runs except for  $T=0.373\ 134$  which is averaged over 54 runs. The curves for  $T=0.328\ 947$  and  $0.321\ 543$  were equilibrated for  $2\times 10^6$  MD time steps before recording the configurations used to calculate  $F_s(k,t)$ . These two curves were averaged over 11 runs. The curve for  $T=0.302\ 114\ 8$  was averaged over 22 runs and was equilibrated for 10 000 MD time steps before recording the configurations used to calculate  $F_s(k,t)$ . The curve for  $T=0.289\ 855$  was averaged over 36 runs and equilibrated for  $50\times 10^6$  MD time steps before recording configurations used to calculate  $F_s(k,t)$ .

where the subscript  $\alpha$  refers to the particle type,  $A$  or  $B$ .  $\vec{r}_i(t)$  is the position of particle  $i$  at time  $t$ , and  $\langle \dots \rangle$  refers to an average over different configurations. The wave vector  $\vec{k}=2\pi\vec{q}/L$  where  $\vec{q}$  is a vector of integers. For an isotropic system  $F_{s,\alpha}(\vec{k},t)$  depends only on the magnitude  $k=|\vec{k}|$ . We will choose  $k=k_{max}$  where  $k_{max}$  is the position of the first maximum of the partial static structure factor  $S_\alpha(k)$ . In Fig. 1 we show the self intermediate scattering function  $F_{s,B}(k,t)$  versus time at temperatures below the caging temperature ( $T\approx 0.4$ ). The caging temperature is the highest temperature at which a plateau is present in the intermediate scattering function versus time. The plateau represents the temporary localization of a particle by a cage of other particles surrounding it.

Mode coupling theory is applicable in the temperature range below the caging temperature and somewhat above the mode coupling  $T_C$ . We define the relaxation time  $\tau_s$  by  $F_s(k,\tau_s)=1/e$ . We determine the relaxation times for the seven highest temperatures shown in Fig. 1 and then fit the

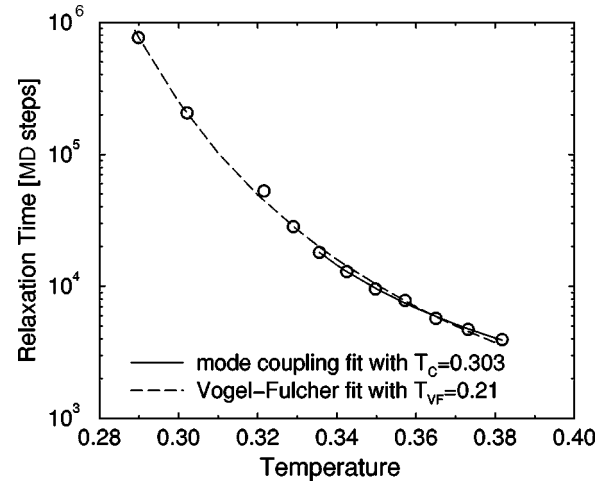


FIG. 2. Relaxation times  $\tau_s$  vs temperature. The solid line is the mode coupling fit to the form  $\tau_s=A(T-T_C)^{-\gamma}$  with  $T_C=0.303$ ,  $\gamma=1.735$ , and  $A=47.6$ . The dashed line is the fit to the Vogel-Fulcher form  $\tau_s(T)=A\exp[B/(T-T_{VF})]$  with  $T_{VF}=0.21$ ,  $A=33.3$ , and  $B=0.803$ .

temperature dependence of  $\tau_s(T)$  to the mode coupling form  $\tau_s(T)\sim(T-T_C)^{-\gamma}$  to find  $T_C$ . For the self part of the intermediate scattering function, the actual value of  $\tau_s$  increases as the magnitude of the wave vector decreases [28]. However, the value of  $T_C$  is independent of  $k$ .  $\tau_s(T)$  versus temperature and the mode coupling fit are shown in Fig. 2. We find the best fit with the mode coupling temperature  $T_C=0.303$  which corresponds to  $\Gamma=1.46$ . Note that  $T_C$  is determined from measurements made at temperatures where the system is equilibrated. Also shown in Fig. 2 is the fit to the Vogel-Fulcher form  $\tau_s(T)=A\exp[B/(T-T_{VF})]$  with  $T_{VF}=0.21$  which corresponds to  $\Gamma=1.60$ . In doing the Vogel-Fulcher fit, we were able to use a much broader range of temperatures since  $T_{VF}$  is much lower than the mode coupling  $T_C$ .

The full intermediate scattering function  $F(\vec{k},t)$  is given by [27]

$$F_\alpha(\vec{k},t)=\frac{1}{N_\alpha}\langle\rho_{\vec{k},\alpha}(t)\rho_{-\vec{k},\alpha}(0)\rangle, \quad (3)$$

where the Fourier transform of the density  $\rho_{\vec{k}}(t)=\sum_{i=1}^N e^{-i\vec{k}\cdot\vec{r}_i(t)}$ . The subscript  $\alpha$  refers to the particle type,  $A$  or  $B$ . The longest  $\alpha$  relaxation time can be determined from the full intermediate scattering function evaluated at  $k=k_{max}$  [29]. We set  $k_{max}=2\pi\times 8.3666/L$  ( $L=8$ ) which is the location of the first peak in the structure factor for type  $B$  particles. We define the  $\alpha$  relaxation time  $\tau$  as the time where  $F_\alpha(k_{max},t)$  decays to  $1/e$ . At a temperature  $T=0.289\ 585\ 8$  which is just below the mode coupling  $T_C$ , we find that  $F_B(k,t)$  has fallen to  $1/e$  at  $\tau=(1.0\pm 0.1)\times 10^6$  MD time steps for a system with 512 particles of which half are type  $B$ . This gives us a time scale by which to compare other times such as our run times. This value of  $\tau$  shows no signs

of aging [30,31] and stays about the same even after  $10^8$  time steps. At higher temperatures this relaxation time is much shorter.

The runs used to determine the intermediate scattering function were done in a slightly different way from the other measurements. These runs were performed at a given temperature and density for  $N_\tau$  MD time steps with no change in temperature or density. The runs were started from a configuration that had been equilibrated at that temperature and density using parallel tempering. The parallel tempering technique is described in the Appendix.

#### IV. SPECIFIC HEAT

The specific heat is a thermodynamic quantity which undergoes a change signaling the glass transition. In experimental systems under constant pressure, the specific heat exhibits a smooth step down as the temperature is lowered through the glass transition. In our simulations, which are done at constant volume, the specific heat has a peak at the glass transition. It is a useful check of our calculation to see if the peak occurs at the same temperature (or density) as the drop in the linear generalized compressibility. There are two ways to compute the specific heat  $C_V$  per particle at a constant volume  $V$ . The first is by taking a derivative of the average energy  $\langle E \rangle$  per particle with respect to temperature:  $C_V = d\langle E \rangle / dT$ . Since we study the system at discrete temperatures, we approximate the derivative by a finite difference,

$$C_V(T_n) = \frac{\langle E(T_n) \rangle - \langle E(T_{n-1}) \rangle}{T_n - T_{n-1}}, \quad (4)$$

where  $T_n > T_{n-1}$  for all integers  $n$ . The second way to calculate the specific heat is from the fluctuations,

$$Nk_B\beta^2(\langle E_P^2 \rangle - \langle E_P \rangle^2), \quad (5)$$

where  $k_B$  is Boltzmann's constant,  $\beta$  is the inverse temperature, and  $E_P$  is the potential energy per particle. In our three dimensional simulations the kinetic energy per particle is given by  $3k_B T/2$ , so it is the fluctuations in the potential energy  $E_P$  per particle which determine the temperature dependence of the specific heat. Thus

$$C_V = \frac{3}{2}k_B + Nk_B\beta^2(\langle E_P^2 \rangle - \langle E_P \rangle^2). \quad (6)$$

In equilibrium, these two ways of calculating the specific heat should agree. So we compare the results of calculating  $C_V$  both ways as a check on our calculation and to make sure the system has equilibrated in all the basins that were visited in the energy landscape.

##### A. Specific heat versus temperature

The specific heat at constant volume exhibits a peak at the glass transition as shown in Fig. 3. The data in this figure are for 512 particles and were averaged over six runs with a measurement time of  $3 \times 10^6$  MD steps. Notice that there is

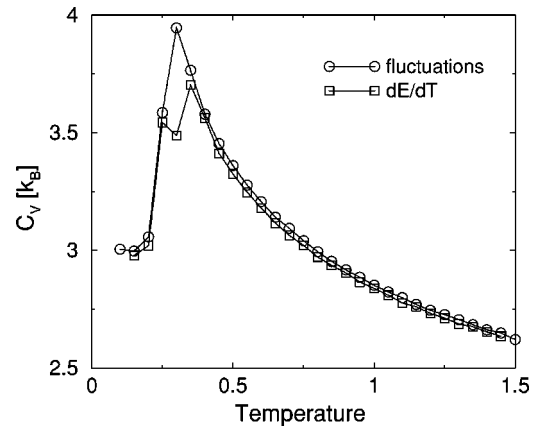


FIG. 3. Specific heat at constant volume as a function of temperature for binary mixture of 512 particles with a measuring time of  $3 \times 10^6$  MD steps averaged over six runs.  $\rho_o = 0.6$  and  $\sigma_B/\sigma_A = 1.4$ . The specific heat is calculated from energy fluctuations and by taking the derivative of the energy with respect to temperature.

good agreement between calculating the specific heat by taking a derivative of the energy with respect to temperature [see Eq. (4)] and by using fluctuations [see Eq. (6)]. This implies that the system has equilibrated within the basins that it visits in the energy landscape. We find similar agreement for other run times. At low temperatures the specific heat goes to  $3k_B$ , as expected for classical oscillators, while at high temperatures  $C_V$  approaches  $3k_B/2$ , which corresponds to an ideal gas. The peak in the specific heat occurs at  $T \approx 0.3$  which corresponds to  $\Gamma \approx 1.46$ . The temperature of the peak coincides with the mode coupling  $T_C = 0.303$  that we deduced from the intermediate scattering function data. Longer run times lead to a sharper peak in the specific heat as can be seen in Fig. 4 which shows the specific heat for 512 particles for several different measuring times. The peaks would presumably be sharper if we had used a finer temperature scale. At high temperatures the agreement between the different times is very good. Perera and Harrowell [32] have

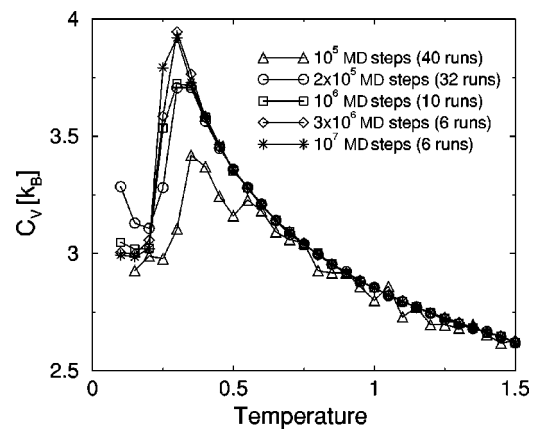


FIG. 4. Specific heat at constant volume as a function of temperature for a binary mixture of 512 particles with measuring times of  $10^5$ ,  $2 \times 10^5$ ,  $10^6$ ,  $3 \times 10^6$ , and  $10^7$  MD time steps. The number of runs averaged over is indicated in the legend. The specific heat is calculated from energy fluctuations.  $\rho_o = 0.6$  and  $\sigma_B/\sigma_A = 1.4$ .

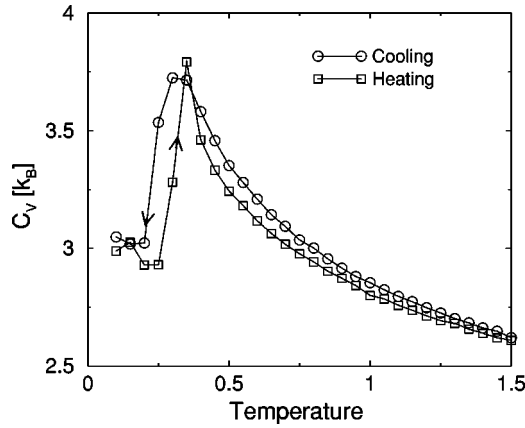


FIG. 5. Specific heat at constant volume during heating and cooling a binary mixture of 512 particles with a measuring time of  $10^6$  MD time steps averaged over ten runs.  $\rho_o=0.6$  and  $\sigma_B/\sigma_A=1.4$ .

found a specific heat peak in a two dimensional binary mixture of soft spheres. They argue that their peak is an equilibrium feature. However, in our case, at temperatures below the peak, the system has fallen out of equilibrium and has become trapped in a basin in the energy landscape. We shall see this later by examining the energy of the inherent structures (potential energy minima) as a function of temperature. Thus the fact that the peak in the specific heat occurs at or very close to the mode coupling  $T_C$  is a result of the relaxation times (see Fig. 2) becoming comparable to and exceeding the simulation run times as the temperature drops below  $T_C$ . When this happens, the system falls out of equilibrium and undergoes a kinetic glass transition.

The specific heat  $C_p$  of experimental systems at constant pressure exhibits a downward step at the glass transition during cooling and a peak at slightly higher temperatures upon heating [33]. As can be seen in Fig. 5, in our warming up simulations, which are done at constant volume, the specific heat peak sharpens and moves toward higher temperatures compared to the cooling runs. This is consistent with what is seen in experiments. The hysteresis is consistent with the system falling out of equilibrium and getting stuck in a basin of the energy landscape.

As we mentioned in the Introduction, some have suggested that the glass transition has an underlying second order phase transition [13–18]. Unlike typical second order phase transitions, there is no experimental evidence that the specific heat diverges at the glass transition. This is consistent with our simulations. In simulations one looks for a divergence by examining whether the quantity increases systematically with system size. In Fig. 6 we plot  $C_V$  for systems with 64, 216, 512, and 1000 particles. As one can see, the specific heat does not exhibit any size dependence. However, we cannot rule out the possibility that a thermodynamic phase transition occurs at temperatures below where we fall out of equilibrium. Indeed theories which postulate a thermodynamic transition put the transition temperature well below the mode coupling  $T_C$ .

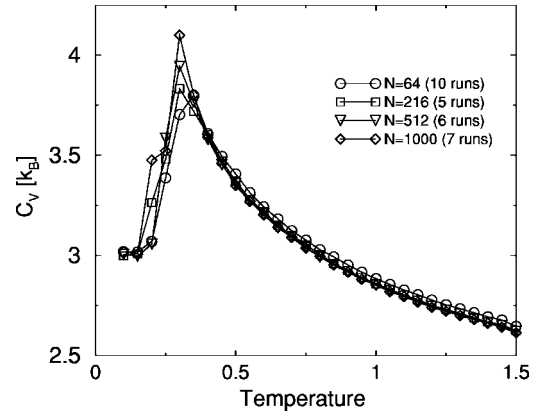


FIG. 6. Specific heat during cooling for binary mixtures of 64, 216, 512, and 1000 particles. The measuring time was  $3 \times 10^6$  MD time steps. The specific heat was calculated from fluctuations and averaged over the number of runs indicated in the legend. Note the lack of size dependence.  $\rho_o=0.6$  and  $\sigma_B/\sigma_A=1.4$ .

### B. Specific heat versus density

In Fig. 7 we show the specific heat as a function of density. As the density increases, the specific heat rises to a peak at  $\rho_o^{\text{peak}}=0.8$ . This corresponds to  $\Gamma=1.44$  which is in good agreement with the  $\Gamma$  value of 1.46 that we found for the specific heat peak when we varied the temperature. Going to higher densities corresponds to going to lower temperatures. At densities higher than 0.8, the system falls out of equilibrium.

### V. GENERALIZED COMPRESSIBILITIES

As we mentioned in the Introduction, the generalized compressibilities are thermodynamic probes that are a function of the microscopic structure of the system. They are solely a function of the positions of the particles and do not depend on their histories. So one could take snapshots of the configurations of the particles at different instances, scramble

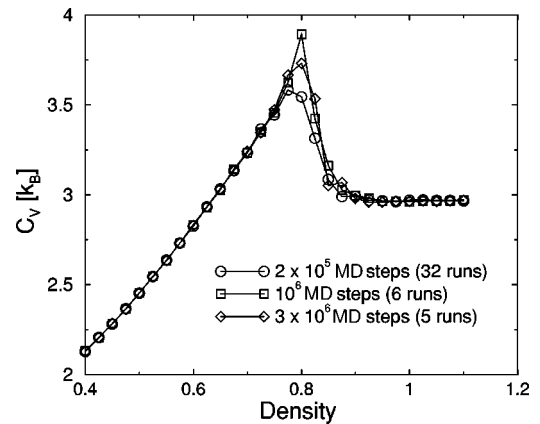


FIG. 7. Specific heat vs density for a binary mixture of 512 particles with  $T=1$ . The measuring times were  $2 \times 10^5$ ,  $10^6$ , and  $3 \times 10^6$  MD time steps. The specific heat was calculated from fluctuations and averaged over the number of runs indicated in the legend.  $\rho_o=0.6$  and  $\sigma_B/\sigma_A=1.4$ .

the order of the snapshots, and still be able to calculate the generalized compressibilities. Averaging over these snapshots corresponds to ensemble averaging. In this sense the generalized compressibilities are thermodynamic quantities which can be calculated solely from the microstates of the system and do not depend on the system's dynamics or kinetics.

We now derive expressions for the linear and nonlinear generalized compressibility. To probe the density fluctuations, we follow the approach of linear response theory and consider applying an external potential  $(\Delta P/\rho_o)\phi(\vec{r})$  which couples to the local density  $\rho(\vec{r}) = \sum_{i=1}^N \delta(\vec{r} - \vec{r}_i)$  where  $\vec{r}_i$  denotes the position of the  $i$ th particle.  $\rho_o$  is the average density.  $\Delta P$  has units of pressure and sets the magnitude of the perturbation.  $\phi(\vec{r})$  is a dimensionless function of position that must be compatible with the periodic boundary conditions imposed on the system, i.e., it must be continuous across the boundaries, but is otherwise arbitrary. This adds to the Hamiltonian  $H$  of the system a term

$$U = \frac{\Delta P}{\rho_o} \int_V d^3r \phi(\vec{r}) \rho(\vec{r}) = \frac{\Delta P}{\rho_o} \sum_i \phi(\vec{r}_i) \equiv \frac{\Delta P}{\rho_o} \rho_\phi, \quad (7)$$

where we have defined  $\rho_\phi = \int_V d^3r \phi(\vec{r}) \rho(\vec{r}) = \sum_i \phi(\vec{r}_i)$ .  $\rho_\phi$  is the inner product of  $\phi$  and  $\rho(\vec{r})$ , and we can regard it as a projection of the density onto a basis function  $\phi(r)$ , i.e.,  $\rho_\phi = \langle \rho | \phi \rangle$ . It weights the density fluctuations according to their spatial position. The application of the external potential will induce an average change  $\delta\rho_\phi$  in  $\rho_\phi$ ,

$$\delta\rho_\phi = \langle \rho_\phi \rangle_U - \langle \rho_\phi \rangle_{U=0}, \quad (8)$$

where the thermal average  $\langle \rho_\phi \rangle_U$  is given by

$$\langle \rho_\phi \rangle_U = \frac{1}{Z} \text{Tr}[e^{-\beta(H+U)} \rho_\phi]. \quad (9)$$

The partition function  $Z = \text{Tr}e^{-\beta(H+U)}$  and  $\beta$  is the inverse temperature. For small values of  $\Delta P$ , this change can be calculated using perturbation theory [34]. Up to third order in  $\Delta P$ , we find

$$\delta\rho_\phi = -\frac{\beta\Delta P}{\rho_o} \langle \rho_\phi^2 \rangle_c + \frac{\beta^2\Delta P^2}{2\rho_o^2} \langle \rho_\phi^3 \rangle_c - \frac{\beta^3\Delta P^3}{6\rho_o^3} \langle \rho_\phi^4 \rangle_c, \quad (10)$$

where the cumulant averages are

$$\langle \rho_\phi^2 \rangle_c = \langle \rho_\phi^2 \rangle - \langle \rho_\phi \rangle^2, \quad (11)$$

$$\langle \rho_\phi^3 \rangle_c = \langle \rho_\phi^3 \rangle - 3\langle \rho_\phi \rangle \langle \rho_\phi^2 \rangle + 2\langle \rho_\phi \rangle^3, \quad (12)$$

$$\begin{aligned} \langle \rho_\phi^4 \rangle_c &= \langle \rho_\phi^4 \rangle - 4\langle \rho_\phi \rangle \langle \rho_\phi^3 \rangle - 3\langle \rho_\phi^2 \rangle^2 + 12\langle \rho_\phi \rangle^2 \langle \rho_\phi^2 \rangle \\ &\quad - 6\langle \rho_\phi \rangle^4, \end{aligned} \quad (13)$$

with the thermal average  $\langle \rho_\phi^n \rangle = \langle \rho_\phi^n \rangle_{U=0}$ . The third order cumulant, Eq. (12), is zero in the liquid phase because for every configuration there exists an equivalent configuration

with the opposite sign of  $(\rho_\phi - \langle \rho_\phi \rangle)$  and so we will not consider this term any further. We can recast Eq. (10) as a power series in the perturbation  $\Delta P$ ,

$$\frac{\delta\rho_\phi}{N} = -\frac{1}{6\rho_o k_B T} \chi_l \Delta P + \frac{1}{6(\rho_o k_B T)^3} \chi_{nl} (\Delta P)^3, \quad (14)$$

where

$$\chi_l = \frac{6}{N} \langle (\rho_\phi)^2 \rangle_c, \quad \chi_{nl} = -\frac{1}{N} \langle (\rho_\phi)^4 \rangle_c. \quad (15)$$

In this paper we will focus our attention on the linear ( $\chi_l$ ) and nonlinear ( $\chi_{nl}$ ) dimensionless generalized compressibilities defined by the above expressions.

We now discuss the choice of the function  $\phi$ . We consider applying the potential along the direction  $\mu$  of one of the coordinate axes so that  $\phi(\vec{r}) = \phi(r^\mu)$ . A natural candidate for  $\phi(r^\mu)$  is  $\cos(k_\mu r^\mu)$  (no implied sum over repeated indices) with  $k_\mu = 2\pi n/L$ , where  $n = 1, 2, \dots$ . In this case,  $\rho_\phi$  is the  $k$ th mode of the cosine transform of the density. We will also consider the simpler function  $\phi(r^\mu) = |r^\mu|/L$ . The absolute value corresponds to the case where all the particles feel a force along the  $\mu$ th direction pointing towards the origin. It gives results very similar to  $\phi(r^\mu) = \cos(k_\mu r^\mu)$  for small  $k$  at a fraction of the computational cost. (No sum over repeated indices.) So our results in this paper correspond to two cases,

$$\rho_\phi = \sum_i |r_i^\mu|/L, \quad (16)$$

which is rather like a center of mass, and

$$\rho_\phi = \sum_i \cos(k_\mu r_i^\mu). \quad (17)$$

Since the system is isotropic, we compute the compressibilities for each direction and then average over the direction  $\mu$ .

In most of our calculations we work in the canonical ensemble where we fix the volume  $V$ , the number  $N$  of particles, and the density  $\rho_o$ . However, it is straightforward to generalize our results to the grand canonical ensemble where the number of particles is not fixed. We simply replace the thermal average defined in Eq. (9) by

$$\langle \rho_\phi \rangle_U = \frac{1}{Z} \sum_N e^{\mu N} \text{Tr}[e^{-\beta(H_N + U_N)} \rho_\phi], \quad (18)$$

where  $\mu$  is the chemical potential,  $H_N$  is the Hamiltonian with  $N$  particles,  $U_N$  is given by Eq. (7) for a system with  $N$  particles, and  $Z$  is the grand canonical partition function given by

$$Z = \sum_N e^{\mu N} \text{Tr}[e^{-\beta(H_N + U_N)}]. \quad (19)$$

The generalized compressibilities can be defined using Eqs. (11) through (15) with the thermal averages  $\langle \rho_\phi^n \rangle = \langle \rho_\phi^n \rangle_{U=0}$  defined in the grand canonical ensemble.

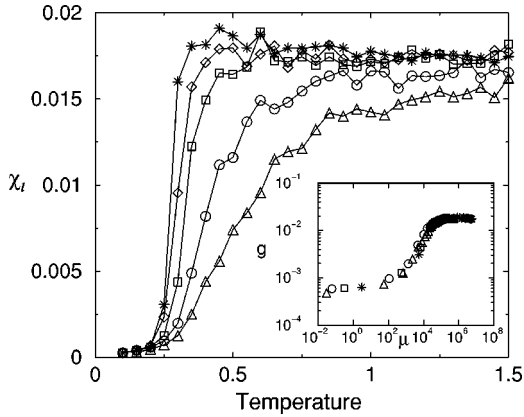


FIG. 8. Linear generalized compressibility as a function of temperature for different measuring times  $t_M$ :  $10^5$  ( $\Delta$ , 40 runs),  $2 \times 10^5$  ( $\circ$ , 32 runs),  $10^6$  ( $\square$ , 10 runs),  $3 \times 10^6$  ( $\diamond$ , 6 runs), and  $10^7$  ( $*$ , 6 runs) MD steps. The system size is 512 particles.  $\rho_o = 0.6$  and  $\sigma_B/\sigma_A = 1.4$ .  $\chi_l$  is calculated using the absolute value of the particles' positions. Inset,  $T > T_o$  subset of the same data scaled as described in text.

### A. Results for linear generalized compressibility

We now turn to our results for the binary glass-forming liquid.

#### 1. $\chi_l$ from absolute value of positions versus temperature

We will first discuss the linear generalized compressibility calculated from the absolute values of the particle positions using Eqs. (15) and (16). Figure 8 shows the linear generalized compressibility as a function of temperature for different run times. The compressibility at high temperatures is independent of  $T$ . In the vicinity of the glass transition  $\chi_l$  drops. Notice that as the measuring time  $t_M$  increases (and hence as the cooling rate decreases), the temperature of the drop decreases and becomes more abrupt. The measuring time can be thought of as the number of snapshots at a single temperature that we use to calculate the compressibility. The linear compressibility is proportional to the width of the distribution of  $\rho_\phi$ , so the drop in  $\chi_l$  corresponds to the sudden narrowing of the distribution  $P(\rho_\phi)$ . If we regard  $\rho_\phi$  as a generalized center of mass, then the drop in  $\chi_l$  signals the sudden arrest in the fluctuations of the generalized center of mass. In other words, at the glass transition the motion of the particles is largely frozen and hence, the generalized center of mass does not move around much. This is consistent with recent observations of the colloidal glass transition in which the size of the clusters of “fast” particles drops dramatically at the glass transition [21].

Notice that at longer measuring times, the temperature  $T_{\text{drop}}$  at which the generalized linear compressibility drops is roughly at the mode coupling temperature  $T_C = 0.303$ . Let us define  $T_{\text{drop}}$  as the temperature at which  $\chi_l$  has dropped half-way down. For  $10^6$  MD steps,  $T_{\text{drop}} \approx 0.33$ ; for  $3 \times 10^6$  MD steps,  $T_{\text{drop}} \approx 0.30$ ; and for  $10^7$  MD steps,  $T_{\text{drop}} \approx 0.27$ . Thus we are able to stay in equilibrium down to the mode coupling temperature for our longer runs. This is what we would expect when we compare these run times, which are longer

than  $1 \times 10^6$  time steps, to the  $\alpha$  relaxation time  $\tau$  which is about  $1 \times 10^6$  time steps at  $T = 0.29$  which is just below  $T_C$ . Thus the fact that the drop in the linear generalized compressibility occurs at or very close to the mode coupling  $T_C$  is a result of the relaxation times (see Fig. 2) becoming comparable to and exceeding the simulation run times as the temperature drops below  $T_C$ . When this happens, the system falls out of equilibrium and undergoes a kinetic glass transition.

The behavior exhibited by  $\chi_l$  can be quantified using a scaling ansatz:  $\chi_l(t_M, T) = g[\mu = t_M/\tau(T)]$ , where the characteristic time has the Vogel-Fulcher form  $\tau(T) = \exp[A/(T - T_o)]$ . The inset of Fig. 8 shows that the data collapse onto a single curve with  $A = 0.75$ ,  $T_o = 0.15$ . (The data could not be fitted using  $\tau(T) = A(T - T_o)^\gamma$  as suggested by simple mode coupling theories [3].) Notice that  $T_o$  lies below the Vogel-Fulcher temperature  $T_{VF} = 0.21$  and the MCT critical temperature  $T_C = 0.303$  deduced by fitting the temperature dependence of the relaxation times. This scaling suggests that  $\chi_l$  becomes a step function for infinite  $t_M$  and that the drop in the compressibility would become a discontinuity at infinitely long times. This abrupt drop is consistent with a sudden arrest of the motion of the particles in the liquid which is the kinetic view of the glass transition. The abrupt drop also appears to be in agreement with Mezard and Parisi's proposal that the glass transition is a first order phase transition with a jump in the specific heat [12,19]. Indeed the temperature at which  $\chi_l$  drops agrees with the temperature of the peak in the specific heat shown in Fig. 4. The specific heat provides an independent check of the glass transition temperature. However, the drop in  $\chi_l$  and the specific heat peak are due to the system falling out of equilibrium, and therefore we cannot really tell if there is an underlying true thermodynamic transition.

One way to see that the system is falling out of equilibrium is to plot the inherent structure energy per particle [9,35,36]. An inherent structure is a particular system configuration whose energy corresponds to the minimum of a basin in the energy landscape. The energy landscape is a  $3N+1$  dimensional surface defined by the potential energy of the system which is a function of the particles' coordinates. During each run we sampled the configurations found at each temperature. Each configuration lies somewhere in a basin and we used the method of conjugate gradients [37] to find the inherent structure energy of that basin. The result is shown in Fig. 9 where we plot the average inherent structure energies versus the temperature of the configuration that was originally saved. At high temperatures the inherent structure energy  $e_{IS}$  per particle is flat as a function of temperature. As the system is cooled,  $e_{IS}$  decreases rather steeply [9]. The inherent structure energy flattens off at low temperatures where the system has fallen out of equilibrium and has become stuck in one basin. For each measuring time the temperature below which the generalized linear compressibility drops corresponds to the temperature below which the inherent structure energy flattens off at low temperatures. Thus the temperature of the drop in  $\chi_l$  and the peak in the specific heat corresponds to the temperature below which the system falls

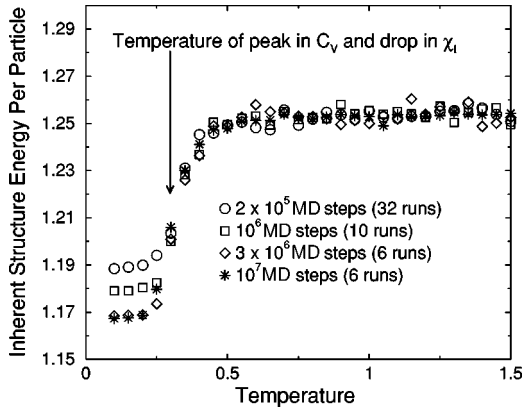


FIG. 9. Inherent structure energy per particle as a function of temperature for a system of 512 particles at different measuring times. Other parameters are the same as in Fig. 8.

out of equilibrium and ceases to explore deeper basins of the energy landscape.

The behavior of the linear generalized compressibility seen in Fig. 8 is similar to that seen in measurements of the real part of the frequency dependent dielectric function  $\varepsilon'(\omega)$  [18]. In that case as the frequency decreased, the temperature of the peak in  $\varepsilon'(\omega)$  decreased and the drop in  $\varepsilon'(\omega)$  below the peak became more abrupt. By extrapolating their data to  $\omega=0$ , Menon and Nagel [18] argued that  $\varepsilon'(\omega=0)$  should diverge at the glass transition, signaling a second order phase transition. We have looked for evidence of this divergence by examining samples of different sizes to see if the linear generalized compressibility increased systematically with system size. As shown in Fig. 10 we find no size dependence and no indication of a diverging linear generalized compressibility. However, as we mentioned earlier, this does not preclude the possibility that a thermodynamic phase transition occurs below  $T_{drop}$ . It simply means that if there is a growing correlation length, it is smaller than the size of our system at  $T > T_{drop}$ . Another possible reason for the absence of size dependence may be that if there is an underlying thermodynamic phase transition, then its order

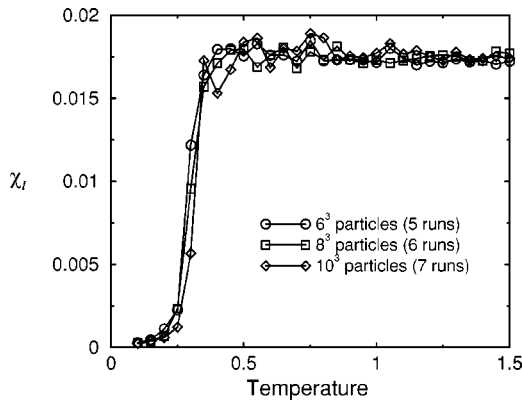


FIG. 10. Linear compressibility as a function of temperature for different system sizes: 216, 512, and 1000 particles. The measuring time was  $3 \times 10^6$  MD steps in all cases. Other parameters are the same as in Fig. 8.

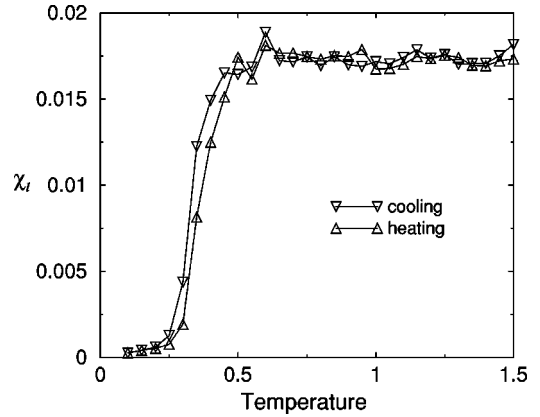


FIG. 11. Linear generalized compressibility as a function of temperature for a binary mixture of 512 particles upon cooling and heating. The measuring time was  $10^6$  MD steps in both cases. The data were averaged over ten runs. Other parameters are the same as in Fig. 8.

parameter may not couple to the local density  $\rho(\vec{r})$ .

So far we have shown the results of cooling the system. In order to look for hysteretic behavior we have done runs in which we heat a system of 512 particles by starting at our lowest temperature  $T=0.1$  with a configuration obtained by cooling the system. We then increased the temperature in steps of  $\Delta T=0.05$ . As before, we equilibrate at each temperature for  $10^4$  time steps and then measure quantities for an additional  $10^6$  time steps. Our results are shown in Fig. 11. Notice the slight hysteresis with the rise in  $\chi_l$  upon warming being at a slightly higher temperature than the drop in  $\chi_l$  upon cooling. This hysteresis is consistent with the kinetic arrest of motion and with the hysteresis found for the specific heat in Fig. 5.

## 2. $\chi_l$ from cosine of positions versus temperature

We now consider calculating the linear generalized compressibility from the cosine transform of the density using Eqs. (15) and (17). So if we apply a cosine potential along, say the  $\mu=x$  direction, then

$$\rho_\phi = \sum_i \cos(k_x x_i), \quad (20)$$

where the wave vector  $k_x = 2\pi n/L$  with  $n=1,2,\dots$ . The wave vectors are compatible with the periodic boundary conditions of our simulations. Since the system is isotropic, we average  $\chi_l$  over the  $x$ ,  $y$ , and  $z$  directions. The resulting linear generalized compressibility is qualitatively similar in its temperature dependence to the linear compressibility calculated using the absolute values of the particles' positions [Eq. (16)]. Figure 12 shows the linear generalized compressibility versus temperature for various values of the wave vector. The data is for a binary mixture of 512 particles with a measuring time of  $10^6$  MD steps and averaged over ten runs. Just as for the absolute value case, we find that as we increase the measuring time, the drop in the linear generalized compressibility calculated using cosine becomes sharper at

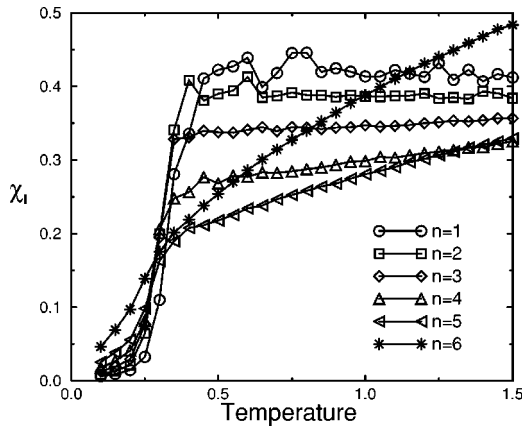


FIG. 12. Linear generalized compressibility as a function of temperature for a binary mixture of 512 particles for different values of the wave vector  $k=2\pi n/L$ . The measuring time was  $10^6$  MD steps in all cases. The data were averaged over ten runs. The susceptibility was calculated using Eqs. (15) and (17). Other parameters are the same as in Fig. 8.

the glass transition. This is shown in Fig. 13 which shows  $\chi_l$  as a function of temperature for measuring times of  $2 \times 10^5$ ,  $10^6$ , and  $3 \times 10^6$  MD steps with  $k=2\pi/L$ , i.e.,  $n=1$ . Figure 14 shows the linear generalized susceptibility versus the wave vector  $k$  in units of  $2\pi/L$  for various temperatures. Note that the dependence is nonmonotonic.

3.  $\chi_l$  versus density

In Fig. 15 we plot the generalized linear compressibility versus density calculated from the absolute value of the positions of the particles. In Fig. 16 we plot the generalized linear compressibility versus density calculated from the cosine of the particles' positions. In both cases we see that  $\chi_l$  drops with increasing density. The drop becomes more abrupt as the measuring time increases. This drop is similar

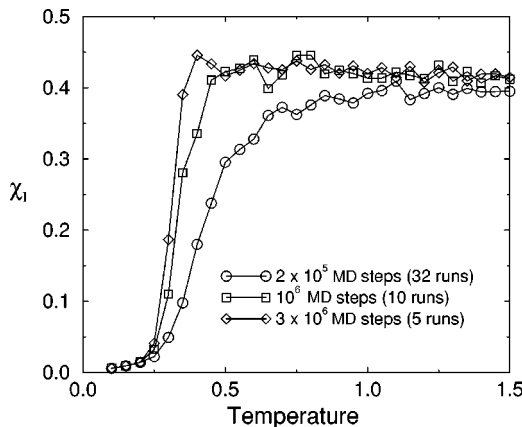


FIG. 13. Linear generalized compressibility as a function of temperature for a binary mixture of 512 particles for different values of the measuring time. The measuring times are  $2 \times 10^5$ ,  $10^6$ , and  $3 \times 10^6$  MD steps. The data were averaged over the number of runs indicated in the legend. The susceptibility was calculated using Eqs. (15) and (17). The wave vector  $k=2\pi/L$ , i.e.,  $n=1$ . Other parameters are the same as in Fig. 12.

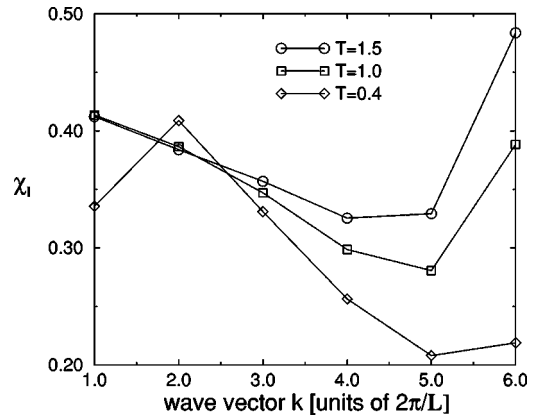


FIG. 14. Linear generalized compressibility as a function of wave vector for a binary mixture of 512 particles for different values of the temperature. The temperature is measured in MD units. The measuring time was  $10^6$  MD steps in all cases. The data were averaged over ten runs. The susceptibility was calculated using Eqs. (15) and (17). Other parameters are the same as in Fig. 12.

to what we see when we cool the system at fixed density. The density ( $\rho \approx 0.8, \Gamma \approx 1.44$ ) at which the drop occurs agrees with the density at which there is a peak in the specific heat as shown in Fig. 7.

4.  $\chi_l$  from absolute value of positions versus temperature in a slab geometry

So far we have considered systems with a fixed number of particles, but as we mentioned earlier in this section, we can generalize our results to the grand canonical ensemble where the number  $N$  of particles can vary. We have examined the generalized linear compressibility  $\chi_l$  calculated from the absolute value of the particle positions using Eqs. (15) and (16) for a slab of our system. In other words we have divided a system of  $8^3$  particles into eight slabs of equal thickness perpendicular to the  $x$  axis. The number of particles in any given slab is not fixed. However, in Eq. (15) we set the

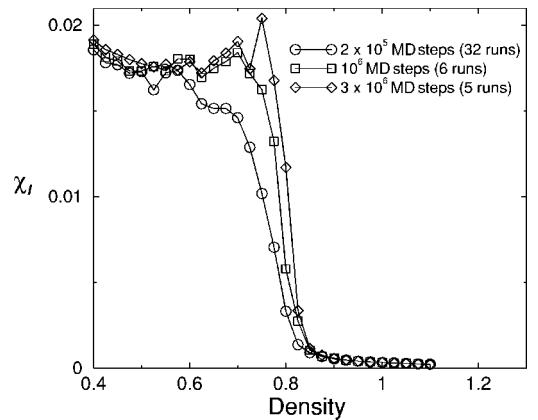


FIG. 15. Generalized linear compressibility as a function of density for a binary mixture of 512 particles at  $T=1$ . The measurement times are  $2 \times 10^5$ ,  $10^6$ , and  $3 \times 10^6$  MD steps.  $\sigma_B/\sigma_A=1.4$ . The data were averaged over the number of runs indicated in the legend.  $\chi_l$  is calculated using the absolute value of the particles' positions.

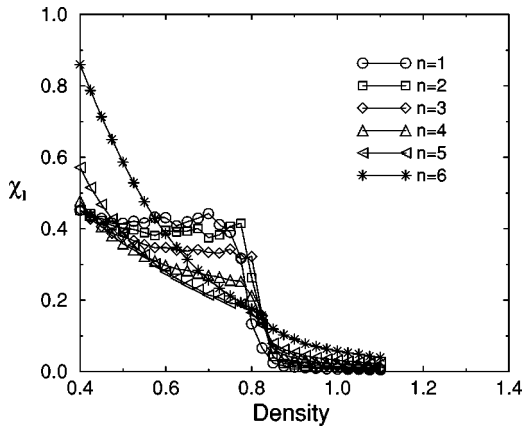


FIG. 16. Generalized linear compressibility as a function of density for a binary mixture of 512 particles at  $T=1$ . The different values of  $n$  correspond to different values of the wave vector  $k = 2\pi n/L$ . The measurement time is  $10^6$  MD steps in all cases.  $\sigma_B/\sigma_A = 1.4$ . The data were averaged over six runs. The susceptibility was calculated from the cosine of the particles' positions using Eqs. (15) and (17). Other parameters are the same as in Fig. 12.

average number  $N$  of particles in each slab equal to the total number of particles in the system divided by the number of layers, i.e.,  $N = 8^3/8 = 64$ . Such a slab geometry mimicks experiments on colloidal suspensions of binary mixtures in which the focal plane of the camera can essentially see only one monolayer of polystyrene balls [38]. In Fig. 17 we show the generalized linear compressibility for a slab for two different measuring times. Again we see that the drop is sharper as the measurement time becomes longer. Thus allowing for fluctuations in the number of particles does not change the qualitative behavior of  $\chi_l$  at the glass transition. Comparing Figs. 8 and 17, we see that the temperature of the drop for the slab and the bulk agree. We also notice that the drop is sharper for the bulk where presumably the greater number of particles results in better statistical averaging.

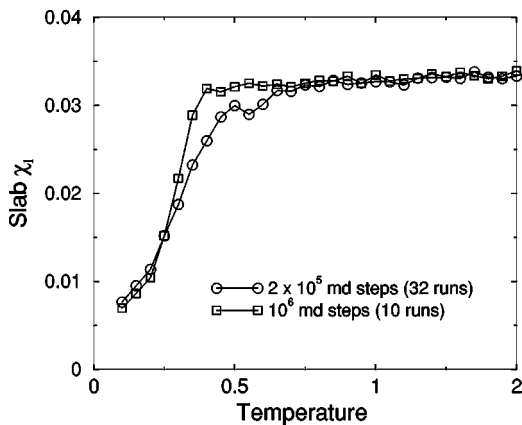


FIG. 17. Linear generalized compressibility as a function of temperature for a monolayer slab in a binary mixture of 512 particles for different values of the measuring time. The measuring times are  $2 \times 10^5$  and  $10^6$  MD steps. The data were averaged over the number of runs indicated in the legend. The susceptibility was calculated using Eqs. (15) and (16). Other parameters are the same as in Fig. 8.

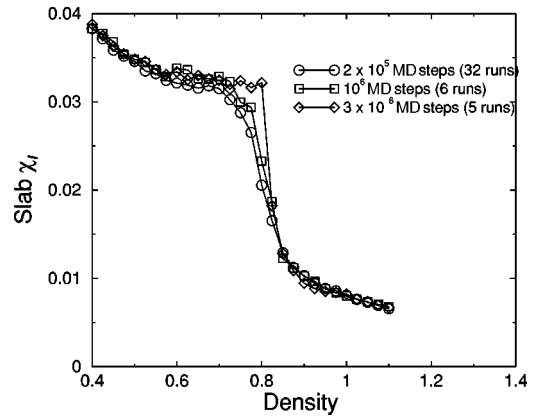


FIG. 18. Linear generalized compressibility as a function of density for a monolayer slab in a binary mixture of 512 particles for different values of the measuring time. The measuring times are  $2 \times 10^5$ ,  $10^6$ , and  $3 \times 10^6$  MD steps. The data were averaged over the number of runs indicated in the legend. The susceptibility was calculated using Eqs. (15) and (16). Other parameters are the same as in Fig. 8.

##### 5. $\chi_l$ from absolute value of positions versus density in a slab geometry

Since experiments on colloidal suspensions usually vary the density rather than the temperature, we have done simulations where we set the temperature  $T=1$  and vary the density. Again we divide our system of  $N = 8^3 = 512$  particles into eight slabs and measure  $\chi_l$  in one of those slabs. The results are shown in Fig. 18. As one can see from the figure,  $\chi_l$  drops as the density is increased and the drop becomes more abrupt as the measuring time lengthens. Comparing Figs. 15, 16, and 18, we see that the drop occurs at the same density ( $\rho \approx 0.8$ ) as in the bulk.

## B. Nonlinear generalized compressibility

We now turn to the case of the nonlinear generalized compressibility  $\chi_{nl}$  given by Eq. (15). We are motivated by the case of spin glasses where the nonlinear magnetic compressibility diverges at the spin glass transition while the linear compressibility only has a cusp [39,40]. There have been a few studies of nonlinear response functions in structural glasses [17,41], but these have not found any divergences. Our results are consistent with this conclusion. In particular, we find that the nonlinear generalized compressibility is zero above and below the glass transition temperature, though it does show a glitch at the glass transition temperature. There is no systematic increase with system size, indicating the absence of a divergence at temperatures above the glass transition. This does not rule out a divergence below the glass transition temperature where our system has fallen out of equilibrium. It also does not rule out a thermodynamic transition that does not couple to the local density. Because  $\chi_{nl}$  is sensitive to the tails of the distribution of  $\rho_\phi$ , one must be careful to obtain a good ensemble average in the liquid above the glass transition temperature. We have done this by doing 16 or 32 runs, each involving 200 000 time steps, with different initial conditions, stringing them together as though

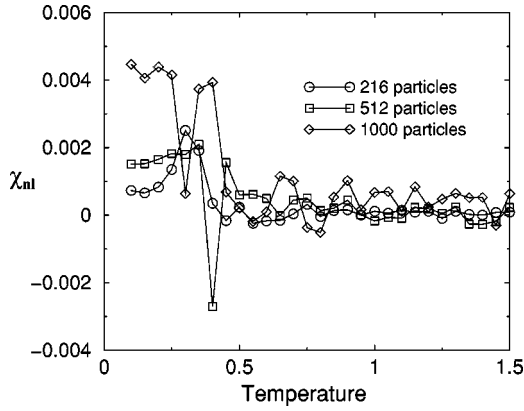


FIG. 19. Nonlinear generalized compressibility as a function of temperature for binary mixtures. The data for 216 particles are from  $3.2 \times 10^6$  MD steps obtained by stringing together 16 runs, each of which involved  $2 \times 10^5$  MD steps. The data for 512 and 1000 particles are from  $6.4 \times 10^6$  MD steps obtained by stringing together 32 runs of  $2 \times 10^5$  MD steps.  $\rho_o = 0.6$  and  $\sigma_B/\sigma_A = 1.4$ .

they were one long run and then taking the appropriate averages. In some sense this approach mixes molecular dynamics and Monte Carlo; the simulation follows the equations of motion for a given amount of time and then “jumps” to another configuration which again evolves according to the molecular dynamics equations until the next jump. We call this approach “global averaging.” It produces a better ensemble average of  $\langle \rho_\phi^2 \rangle^2$  which enters into  $\chi_{nl}$  in Eq. (13). The resulting  $\chi_{nl}$  is shown in Fig. 19 which was calculated from the absolute values of the particles’ positions using Eqs. (15) and (16).

$\chi_{nl}$  also took longer to equilibrate than  $\chi_l$ . By plotting  $\chi_{nl}$  versus run time, we found that one had to run at least  $10^6$  time steps at  $T=1$  before  $\chi_{nl}$  appeared to saturate (see Fig. 20).

## VI. ORDINARY ISOTHERMAL COMPRESSIBILITY

The ordinary isothermal compressibility  $\kappa_T$  can be related to the fluctuations in the number, volume, or density of the

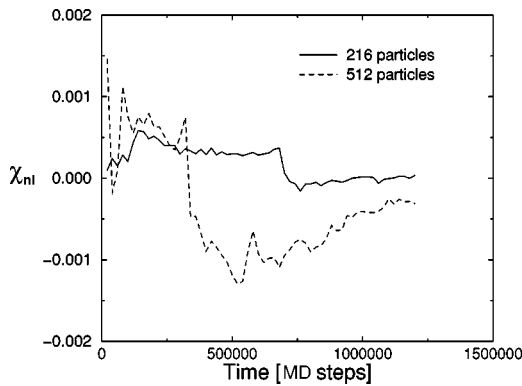


FIG. 20. Nonlinear generalized compressibility as a function of time for binary mixtures of 216 and 512 particles at  $T=1$ . The data shown for each system size are for a single run and a running average is kept.  $\chi_{nl}$  is calculated using Eqs. (15) and (16).  $\rho_o = 0.6$  and  $\sigma_B/\sigma_A = 1.4$ .

system. In most of our calculations we fix the volume, number of particles, and density, so that there are no such fluctuations and the system has  $\kappa_T=0$ . However, in the grand canonical ensemble  $\kappa_T$  is given by

$$\kappa_T = \frac{1}{\rho_o k_B T} \frac{\langle N^2 \rangle - \langle N \rangle^2}{\langle N \rangle}, \quad (21)$$

where  $\rho_o = \langle N \rangle / V$ . To relate  $\kappa_T$  to the linear generalized compressibility  $\chi_l$ , we choose a uniform potential  $\phi(\vec{r}) = 1$ . Then  $\rho_\phi = \int d^3 r \rho(\vec{r}) = N$  and

$$\kappa_T = \frac{1}{6 \rho_o k_B T} \chi_l. \quad (22)$$

In principle, one can also obtain  $\kappa_T$  from the  $k \rightarrow 0$  limit of the static structure factor  $S(\vec{k}) = (1/N) \langle \rho_{\vec{k}} \rho_{-\vec{k}} \rangle$  where  $\rho_{\vec{k}} = \sum_{i=1}^N \exp(-i\vec{k} \cdot \vec{r}_i)$  is the Fourier transform of the local density  $\rho(\vec{r})$ . The limit of  $S(\vec{k})$  for  $k \rightarrow 0$  in an isotropic and homogeneous system is [27]

$$S(0) = 1 + \rho_o \int (g(r) - 1) d^3 r = \rho_o k_B T \kappa_T, \quad (23)$$

where  $g(r)$  is the radial distribution function. Note that in a system with fixed volume and particle number, the normalization of  $g(r)$  leads to  $S(k \rightarrow 0) = 0$ . This is consistent with the fact that such a system has  $\kappa_T = 0$ . Equation (23) yields a nonzero value for  $\kappa_T$  in a system which has fluctuations in volume, particle number, or density. Even in such a compressible system taking the  $k \rightarrow 0$  limit of  $S(k)$  can suffer from finite size effects [42] because the farthest apart that any two particles can be along any given coordinate axis is  $L/2$  when there are periodic boundary conditions. So at wave vectors  $k$  with components smaller than  $4\pi/L$ ,  $S(k)$  can have spurious results. [For example, in our simulations we found that this manifests itself as a slight upturn in  $S(k)$  at small  $k$ .] It is possible to extrapolate to distances larger than  $L/2$  using various approaches [42]. We chose not to use this approach to calculate  $\kappa_T$  since we work in a system with fixed  $N$  and  $V$ . We should note, however, that simulations [43] working in the  $NVT$  ensemble with fixed  $N$ ,  $V$ , and  $T$ , have successfully used Eq. (23) to find the isothermal compressibility. We can resolve this with the fact that  $S(k \rightarrow 0) = 0$  in the  $NVT$  ensemble by noting that for values of  $k > 4\pi/L$ ,  $S(k)$  should give the same value in the  $NVT$  ensemble as in the grand canonical ensemble. So if  $L$  is large enough, fitting  $S(k)$  to the small  $k$  form  $S(k) = S(k \rightarrow 0) + Ak^2$ , where  $A$  is a constant, should yield the correct value of  $\kappa_T$  as long as  $k > 4\pi/L$ .

Rather than using Eq. (23), we calculated  $\kappa_T$  by monitoring a small subvolume inside of our system and keeping track of the fluctuations in the number of particles in the subvolume. Let us define a dimensionless ordinary isothermal compressibility  $K_T$  by

$$\kappa_T = \frac{1}{\rho_o k_B T} K_T, \quad (24)$$

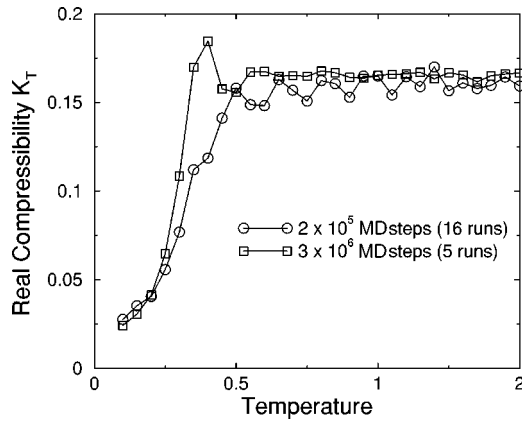


FIG. 21. Dimensionless ordinary isothermal compressibility  $K_T$  as a function of temperature for a subset of a system of 512 particles for different values of the measuring time. On average, the subset had 128 particles in it. The measuring times are  $2 \times 10^5$  and  $3 \times 10^6$  MD steps. The data were averaged over the number of runs indicated in the legend. The dimensionless compressibility was calculated using Eq. (25). Other parameters are the same as in Fig. 8.

where

$$K_T = \frac{\langle N^2 \rangle - \langle N \rangle^2}{\langle N \rangle}. \quad (25)$$

In order to calculate  $K_T$ , we have monitored a subvolume that had on average 25% of the total number of particles. Essentially we drew an imaginary boundary in the middle of our system that enclosed 25% of the total volume and counted the number of particles in this subvolume as a function of time. By monitoring the fluctuations in the number of particles in this subvolume, we could calculate  $K_T$ . The results for a subvolume which had on average 128 particles out of a total of 512 particles are shown in Fig. 21 where  $K_T$  is plotted versus temperature. We see that it has the same basic shape as the linear generalized compressibility with a drop at the same temperature as  $\chi_l$ . As with  $\chi_l$ , the drop becomes sharper with increasing measuring time.

While  $K_T$  shows behavior similar to the linear generalized compressibility  $\chi_l$  as a function of temperature for a given size, it is unlike  $\chi_l$  in that it suffers from finite size effects. We have demonstrated this by making measurements on systems with a total of 64, 216, 512, and 1000 particles. The measurements were made by counting the number of particles in a subvolume that was 25% of the total volume. Such a small subvolume has a large surface to volume ratio which produces large finite size effects. To understand this, we note that in such a small subvolume, a significant number of the particles are very close to the boundary of the subvolume. Fluctuations in the positions of these particles moves them in and out of the subvolume, producing large fluctuations in the number of particles in the subvolume. The smaller the system, the bigger this effect is. This produces large finite size effects in  $K_T$  even at high temperatures where the system easily equilibrates. This can be seen in Fig. 22. One can see that  $K_T$  decreases with increasing system size at high temperatures above the drop in the compressibility. One of the

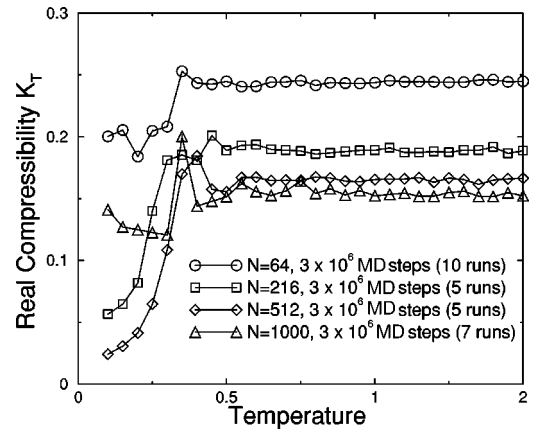


FIG. 22. Dimensionless ordinary isothermal compressibility  $K_T$  as a function of temperature for systems with a total of  $N = 64$ , 216, 512, and 1000 particles. The isothermal compressibility was obtained by monitoring a subvolume that had on average 25% of the particles in it. Notice the size dependence at high temperatures. The measuring time is  $3 \times 10^6$  MD steps. The data were averaged over the number of runs indicated in the legend. The dimensionless compressibility was calculated using Eq. (25). Other parameters are the same as in Fig. 8.

advantages of the linear generalized compressibility is the absence of these finite size effects. In fact, the linear generalized compressibility shows no size dependence at temperatures above the observed glass transition (see Fig. 10).

## VII. DIFFUSION CONSTANT

The diffusion of the particles reflects the kinetics of the system and becomes very small below the glass transition temperature. We calculate the diffusion constant  $D$  using the Einstein relation

$$D = \lim_{t \rightarrow \infty} \frac{1}{6Nt} \left\langle \sum_{i=1}^N [\mathbf{r}_i(t) - \mathbf{r}_i(0)]^2 \right\rangle, \quad (26)$$

where  $\mathbf{r}_i$  are true displacements of the  $i$ th particle. Since we are using periodic boundary conditions, if the particle has crossed the box several times, then this must be included in  $\mathbf{r}_i$ .

### A. Diffusion constant versus temperature

As the system is cooled through the glass transition, the diffusion constant calculated using Eq. (26) becomes very small. This is shown in Fig. 23 where the diffusion constant for 512 particles is plotted on a logarithmic scale. The diffusion constant varies smoothly over the entire temperature range. The curves corresponding to different cooling rates begin to separate as the system falls out of equilibrium at the glass transition temperature where the specific heat peaks and where the linear generalized compressibility drops abruptly. Figure 23 also shows the diffusion constant for binary mixtures of several different sizes. Notice that there is no apparent size effect.

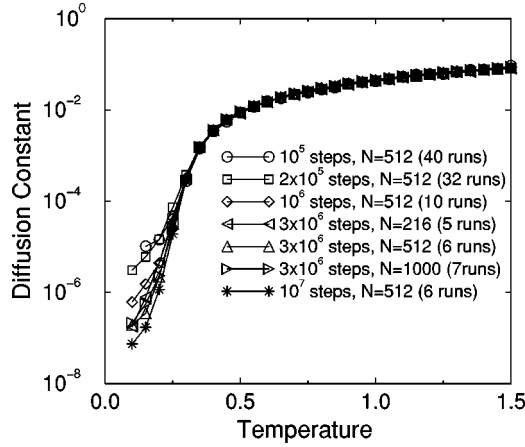


FIG. 23. Diffusion constant as a function of temperature for a binary mixture of particles plotted on a logarithmic scale. Measurement times for 512 particles are  $10^5$ ,  $2 \times 10^5$ ,  $10^6$ ,  $3 \times 10^6$ , and  $10^7$  MD steps. Measurement time for 216, 512, and 1000 particles is  $3 \times 10^6$  MD steps. Number of runs averaged over is given in the legend.  $\rho_o = 0.6$  and  $\sigma_B/\sigma_A = 1.4$ .

### B. Diffusion constant versus density

In Fig. 24 we show the diffusion constant as a function of density. We see that the diffusion decreases smoothly as the density  $\rho$  increases. The curves corresponding to different measurement times begin to separate at the glass transition density where the specific heat peaks and where the linear generalized compressibility drops abruptly.

## VIII. RELATION BETWEEN $\chi_l$ AND $S(k)$

When the system has translational invariance, we can relate the linear generalized compressibility  $\chi_l$  to the static structure factor  $S(k)$  which is measured in experiments such as neutron scattering.  $S(k)$  is also used as an input for mode coupling theories [3] and it is generally assumed that  $S(k)$  does not show any essential variations near the glass transi-

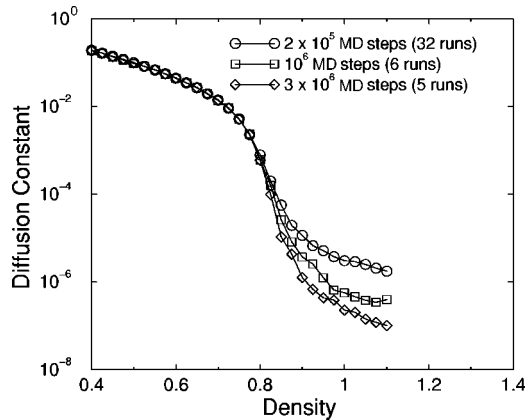


FIG. 24. Logarithmic plot of the diffusion constant as a function of density for a binary mixture of 512 particles at  $T = 1$ . The measurement times are  $2 \times 10^5$ ,  $10^6$ , and  $3 \times 10^6$  MD steps.  $\sigma_B/\sigma_A = 1.4$ . The data were averaged over the number of runs indicated in the legend.

tion as the temperature or density is varied. As we shall see, our calculation agrees with this.

By definition, the static structure factor  $S(\vec{k}) = (1/N) \times \langle \rho_{\vec{k}} \rho_{-\vec{k}} \rangle$ . To relate  $S(k)$  to  $\chi_l$ , we first note that  $S(k)$  is the Fourier transform of the static density-density autocorrelation function  $G(\vec{r})$ , i.e.,  $S(\vec{k}) = \int \exp(-i\vec{k} \cdot \vec{r}) G(\vec{r}) d^3 r$ , where  $G(\vec{r}) = (1/N) \int \langle \rho(\vec{r}' + \vec{r}) \rho(\vec{r}') \rangle d^3 r'$ . In the supercooled liquid above the glass transition, the system has translational invariance, and we can write

$$\langle \rho(\vec{r}) \rho(\vec{r}') \rangle = \frac{1}{V} g(\vec{r} - \vec{r}'), \quad (27)$$

where  $V$  is volume and  $g$  is a function of the difference  $(\vec{r} - \vec{r}')$ . In this case  $G(\vec{r}) = g(\vec{r})/N$ . In  $\chi_l$  we meet

$$\langle \rho_\phi^2 \rangle = \int d^3 r d^3 r' \phi(\vec{r}) \phi(\vec{r}') \langle \rho(\vec{r}) \rho(\vec{r}') \rangle. \quad (28)$$

If there is translational invariance,

$$\begin{aligned} \langle \rho_\phi^2 \rangle &= \frac{1}{V} \int d^3 r d^3 r' \phi(\vec{r}) \phi(\vec{r}') g(\vec{r} - \vec{r}') \\ &= \frac{1}{V} \int \frac{d^3 k}{(2\pi)^3} \phi(\vec{k}) \phi(-\vec{k}) g(-\vec{k}) \\ &= \rho_o \int \frac{d^3 k}{(2\pi)^3} |\phi(\vec{k})|^2 S(\vec{k}), \end{aligned} \quad (29)$$

where  $\phi(\vec{k})$  is the Fourier transform of  $\phi(\vec{r})$ . Converting the integral  $V \int d^3 k / (2\pi)^3$  to a sum  $\sum_{\vec{k}}$  and using Eq. (15), we obtain

$$\chi_l = \frac{6}{N} \left[ \frac{N}{V^2} \sum_{\vec{k}} [|\phi(\vec{k})|^2 S(\vec{k})] - \langle \rho_\phi \rangle^2 \right]. \quad (30)$$

As an example, let us choose  $\phi(\vec{r}) = \cos(k_x x)$  with the proviso that  $k_x \neq 0$ . (When  $\vec{k} = 0$ ,  $\chi_l = 0$  since the potential is uniform and there are no fluctuations allowed with fixed  $N$  and  $V$ .) With this choice of  $\phi(\vec{r})$ ,  $\rho_\phi = \sum_i \cos(k_x x_i)$ . Then one can show by explicitly calculating  $\phi(\vec{k})$  and by using Eqs. (29) and (30) that

$$\chi_l(\vec{k}) = 3S(\vec{k}) - \frac{6}{N} [\text{Re} \langle \rho_{\vec{k}} \rangle]^2, \quad (31)$$

where translational invariance allows us to write

$$S(\vec{k}) = (2/N) \langle \rho_\phi^2 \rangle = (2/N) \sum_{ij} [\langle \cos(k_x x_i) \cos(k_x x_j) \rangle]. \quad (32)$$

Note that the value of  $k$  that we use to probe the glass transition is typically of order  $k_L \equiv 2\pi/L$  which is much smaller

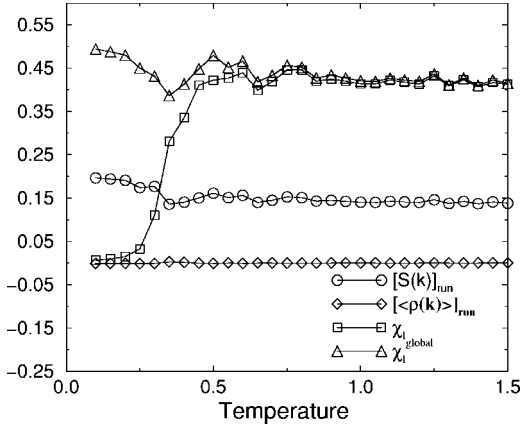


FIG. 25. Linear generalized compressibility  $\chi_l$ , static structure factor  $[S(k)]_{\text{run}}$ ,  $[\text{Re}(\rho_k)]_{\text{run}}$ , linear generalized compressibility  $\chi_l$  averaged run by run, and the globally averaged linear generalized compressibility  $\chi_l^{\text{global}}$  vs temperature for a binary mixture of 512 particles. The measurement time was  $10^6$  MD steps for each temperature. The data were averaged over ten runs and over  $\vec{k} = (2\pi/L, 0, 0)$ ,  $\vec{k} = (0, 2\pi/L, 0)$ , and  $\vec{k} = (0, 0, 2\pi/L)$ .  $\rho_o = 0.6$  and  $\sigma_B/\sigma_A = 1.4$ .

than the value of  $k_{\text{peak}}$  at which the first peak in  $S(k)$  appears.  $k_{\text{peak}} \sim 2\pi/\sigma_A \gg k_L$  where  $\sigma_A$  is the diameter of type A spheres in the binary mixture.

We have numerically calculated  $[S(k)]_{\text{run}}$  for our binary mixture using Eq. (32) with  $\phi(r) = \cos(k_\mu r_\mu)$ . (No sum over repeated indices.  $\mu = x, y, \text{ or } z$ .)  $[\dots]_{\text{run}}$  is an average over all the runs and over  $\vec{k}$  being parallel to  $x, y, \text{ and } z$ . The result is shown in Fig. 25 and one can see that  $[S(k)]_{\text{run}}$  does not vary much through the glass transition which is consistent with what is assumed in mode coupling theory. The figure also shows  $[\text{Re}(\rho_k)]_{\text{run}}$  where  $\langle \dots \rangle$  is a thermal average over a single run. If  $[S(k)]_{\text{run}}$  and  $[\text{Re}(\rho_k)]_{\text{run}}$  do not vary much through the glass transition, how can the difference between the two terms in Eq. (31) decrease and produce a drop in  $\chi_l$ ? To answer this, note that there are two inequivalent ways in which one can calculate  $\chi_l$ . So far we have calculated  $\chi_l$  for each run and then averaged over the different runs. This approach is what we used in Figs. 8–11 and results in a sharp drop in the linear generalized compressibility at the glass transition. Let us call this a run-by-run average for which we can write

$$\chi_l = \frac{6}{N} [\langle \rho_\phi^2 \rangle - \langle \rho_\phi \rangle^2]_{\text{run}}. \quad (33)$$

The drop in  $\chi_l$  comes about because the width of the distribution of  $\text{Re}(\rho_\phi)$  becomes much smaller below the transition. At low temperatures, structural arrest hinders the exploration of phase space and reduces the fluctuations in  $\text{Re}(\rho_\phi)$ .

The other way to calculate the generalized linear compressibility is with global averaging in which we string together a series of separate runs, treat it as one giant run, and then do the averaging required to calculate the generalized linear compressibility  $\chi_l^{\text{global}}$ .

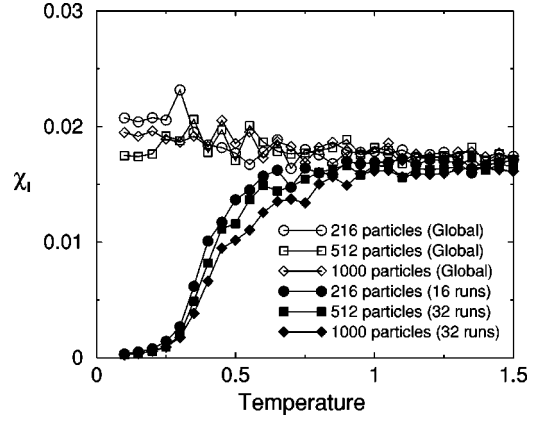


FIG. 26. Linear generalized compressibility as a function of temperature for binary mixtures of 216, 512, and 1000 particles. The filled symbols correspond to calculating  $\chi_l$  for each run with a measuring time of  $2 \times 10^5$  MD steps and then averaging over the number of runs indicated in the legend, while the open symbols correspond to global averages (stringing all these runs together to get one big “run” for a given system size). So the global average for 216 particles uses  $3.2 \times 10^6$  MD steps while for 512 and 1000 particles,  $6.4 \times 10^6$  MD steps were used.  $\chi_l$  is calculated using Eqs. (15) and (16).  $\rho_o = 0.6$  and  $\sigma_B/\sigma_A = 1.4$ .

$$\chi_l^{\text{global}} = \frac{6}{N} \{ [\langle \rho_\phi^2 \rangle]_{\text{run}} - ([\langle \rho_\phi \rangle]_{\text{run}})^2 \}. \quad (34)$$

Careful inspection of Eqs. (33) and (34) reveals that the difference is in whether we square the thermal average  $\langle \rho_\phi \rangle$  and then average over runs to obtain  $[\langle \rho_\phi \rangle]_{\text{run}}$  in  $\chi_l$ , or average  $\langle \rho_\phi \rangle$  over runs and then square it to obtain  $([\langle \rho_\phi \rangle]_{\text{run}})^2$  in  $\chi_l^{\text{global}}$ . If we now return to Fig. 25 and take the difference of  $[S(k)]_{\text{run}}$  and  $([\text{Re}(\rho_k)]_{\text{run}})^2$ , we obtain the global average

$$\chi_l^{\text{global}} = 3[S(k)]_{\text{run}} - \frac{6}{N} ([\text{Re}(\rho_k)]_{\text{run}})^2. \quad (35)$$

The result of both types of averaging is shown in Figs. 25 and 26. Notice that  $\chi_l^{\text{global}}$  does not exhibit a drop with decreasing temperature while  $\chi_l$  does. To understand why there is no drop in  $\chi_l^{\text{global}}$ , note that by combining several different runs, very different configurations are sampled which produces much larger fluctuations in the generalized center of mass at low temperatures compared to  $\chi_l$ . As a result  $\chi_l^{\text{global}}$ , which is a measure of the size of these fluctuations, does not have an abrupt drop.

## IX. SUMMARY

To summarize, we have introduced a quantity called the generalized compressibility which depends solely on the positions of the particles and not on their histories. The generalized compressibility can easily be calculated in the canonical (e.g.,  $NVT$ ) and grand canonical ensembles. In particular, it is well defined in a system which has particle number and volume fixed. In addition, it does not suffer from the finite size effects often encountered in calculating the ordinary

compressibility. The linear generalized compressibility drops abruptly at the observed glass transition due to the kinetic arrest of motion. This makes it a good quantity to calculate or measure in order to find the observed glass transition as a function of density or temperature. The generalized compressibility can be experimentally measured in several ways. It can be directly measured in colloidal experiments which monitor the positions of the particles. Measurements of the width of the distribution of  $\rho_{\vec{k}}$ , the spatial Fourier transform of the density, would also yield the linear generalized compressibility.

#### ACKNOWLEDGMENTS

We thank Sharon Glotzer, Walter Kob, Andrea Liu, and Francesco Sciortino for helpful discussions. This work was supported in part by DOE Grant No. DE-FG03-00ER45843 as well as by CULAR funds provided by the University of California for the conduct of discretionary research by Los Alamos National Laboratory.

#### APPENDIX: PARALLEL TEMPERING

In calculating the intermediate scattering function at a given temperature, we initialized the run using a configuration at that temperature generated by parallel tempering. In this appendix we briefly describe the parallel tempering method.

We implement parallel tempering [44–47] by choosing

the temperatures at which we wish to have measurements made. We then run molecular dynamics simulations in parallel at these temperatures using a temperature constraint algorithm [25] to keep the temperature of each simulation constant. At 100 time step intervals we attempt to switch the configurations of two neighboring temperatures using a Metropolis test which ensures that the energies of the configurations sampled at any given temperature have a Boltzmann distribution. Let  $\beta_1$  and  $\beta_2$  be two neighboring inverse temperatures, and let  $U_1$  and  $U_2$  be the corresponding potential energies of the configurations at these temperatures at a time step just before the possible swap. If  $\Delta = (\beta_1 - \beta_2)(U_2 - U_1)$ , then the switch is accepted with probability unity if  $\Delta \leq 0$  and with probability  $\exp(-\Delta)$  if  $\Delta > 0$ . The temperatures are chosen so that the acceptance ratio is between 30% and 75%. At the temperatures in the vicinity of the mode coupling  $T_C$ , the acceptance ratio was typically above 75% for  $L=6$  and above 60% for  $L=8$ . After a swap is accepted, the velocities of the particles in each configuration are rescaled to suit their new temperature. Each configuration is then evolved using molecular dynamics for another 100 time steps. Switching configurations allows a given simulation to do a random walk in temperature space in which it visits both low temperatures and high temperatures. This helps to prevent a simulation from becoming trapped in a valley of the energy landscape at low temperatures. Typically we equilibrate for  $2 \times 10^6$  time steps and then do measurements for an additional  $4 \times 10^6$  time steps.

- 
- [1] M.D. Ediger, C.A. Angell, and S.R. Nagel, *J. Phys. Chem.* **100**, 13 200 (1996), and references therein.
- [2] J. T. Fourkas, D. Kivelson, U. Mohanty, and K. A. Nelson, *Supercooled Liquids: Advances and Novel Applications* (American Chemical Society, Washington, D.C., 1997).
- [3] W. Götze and L. Sjögren, *Rep. Prog. Phys.* **55**, 241 (1992).
- [4] C. Donati *et al.*, *Phys. Rev. Lett.* **80**, 2338 (1998).
- [5] R. Yamamoto and A. Onuki, *Europhys. Lett.* **40**, 61 (1997).
- [6] R. Yamamoto and A. Onuki, *J. Phys. Soc. Jpn.* **66**, 2545 (1997).
- [7] U. Tracht *et al.*, *Phys. Rev. Lett.* **81**, 2727 (1998).
- [8] M. Goldstein, *J. Chem. Phys.* **51**, 3728 (1969).
- [9] S. Sastry, P.G. Debenedetti, and F.H. Stillinger, *Nature (London)* **393**, 554 (1998).
- [10] G. Adam and J.H. Gibbs, *J. Chem. Phys.* **43**, 139 (1965).
- [11] J.H. Gibbs and E.A. DiMarzio, *J. Chem. Phys.* **28**, 373 (1958).
- [12] M. Mézard and G. Parisi, *Phys. Rev. Lett.* **82**, 747 (1999).
- [13] T.R. Kirkpatrick, D. Thirumalai, and P.G. Wolynes, *Phys. Rev. A* **40**, 1045 (1989).
- [14] J.P. Sethna, J.D. Shore, and M. Huang, *Phys. Rev. B* **44**, 4943 (1991).
- [15] D. Kivelson *et al.*, *Physica A* **219**, 27 (1995).
- [16] R.M. Ernst, S.R. Nagel, and G.S. Grest, *Phys. Rev. B* **43**, 8070 (1991).
- [17] C. Dasgupta, A.V. Indrani, S. Ramaswamy, and M.K. Phani, *Europhys. Lett.* **15**, 307 (1991).
- [18] N. Menon and S.R. Nagel, *Phys. Rev. Lett.* **74**, 1230 (1995).
- [19] G. Parisi, in *Complex Behaviour of Glassy Systems*, edited by M. Rubi and C. Perez-Vicente (Springer-Verlag, Berlin, 1997), pp. 111–121.
- [20] J. Yvon, *Nuovo Cimento, Suppl.* **9**, 144 (1958).
- [21] E.R. Weeks *et al.*, *Science* **287**, 627 (2000).
- [22] H.M. Carruzzo and C.C. Yu, *Philos. Mag. B* **82**, 125 (2002).
- [23] T.A. Weber and F.H. Stillinger, *Phys. Rev. B* **31**, 1954 (1985).
- [24] W. Kob and H.C. Andersen, *Phys. Rev. Lett.* **73**, 1376 (1994).
- [25] D. C. Rapaport, *The Art of Molecular Dynamics Simulation* (Cambridge University Press, New York, 1995).
- [26] J.-L. Barrat, J.-N. Roux, and J.-P. Hansen, *Chem. Phys.* **149**, 197 (1990).
- [27] J. P. Hansen and I. R. McDonald, *Theory of Simple Liquids*, 2nd ed. (Academic Press, London, 1986).
- [28] W. Kob and H.C. Andersen, *Phys. Rev. E* **52**, 4134 (1995).
- [29] A. Rinaldi, F. Sciortino, and P. Tartaglia, *Phys. Rev. E* **63**, 061210 (2001).
- [30] W. Kob and J.L. Barrat, *Phys. Rev. Lett.* **78**, 4581 (1997).
- [31] W. Kob and J.L. Barrat, *Eur. Phys. J. B* **13**, 319 (2000).
- [32] D.N. Perera and P. Harrowell, *Phys. Rev. E* **59**, 5721 (1999).
- [33] M.A. DeBolt, A.J. Easteal, P.B. Macedo, and C.T. Moynihan, *J. Am. Ceram. Soc.* **59**, 16 (1976).
- [34] M. Toda, N. Saito, R. Kubo, and N. Hashitsume, *Statistical Physics II: Nonequilibrium Statistical Mechanics*, 2nd ed. (Springer-Verlag, Berlin, 1991).
- [35] F.H. Stillinger and T.A. Weber, *Phys. Rev. A* **25**, 978 (1982).
- [36] F.H. Stillinger and T.A. Weber, *Science* **225**, 983 (1984).

- [37] W. H. Press, S. A. Teukolsky, W. T. Vetterling, and B. P. Flannery, *Numerical Recipes in C: The Art of Scientific Computing* (2nd ed.) (Cambridge University Press, Cambridge, UK, 1992), p. 420.
- [38] C. A. Murray (private communication).
- [39] R.N. Bhatt and A.P. Young, *Phys. Rev. B* **37**, 5606 (1988).
- [40] L.P. Levy and A.T. Ogielski, *Phys. Rev. Lett.* **57**, 3288 (1986).
- [41] L. Wu, *Phys. Rev. B* **43**, 9906 (1991).
- [42] B. Bernu, Y. Hiwatari, and J.P. Hansen, *J. Phys. C* **18**, L371 (1985).
- [43] J. Horbach and W. Kob, *Phys. Rev. B* **60**, 3169 (1999).
- [44] K. Hukushima and K. Nemoto, *J. Phys. Soc. Jpn.* **65**, 1604 (1996).
- [45] K. Hukushima, H. Takayama, and H. Yoshino, *J. Phys. Soc. Jpn.* **67**, 12 (1998).
- [46] W. Kob, C. Brangian, T. Stuhn, and R. Yamamoto, in *Computer Simulation Studies in Condensed Matter Physics XIII*, edited by D. P. Landau, S. P. Lewis, and H. B. Schuttler (Springer-Verlag, Berlin, 2001), p. 153.
- [47] C.D. Michele and F. Sciortino, e-print cond-mat/01112056 (2001).